Additive Manufacturing Letters 1 (2021) 100017

Contents lists available at ScienceDirect

Additive Manufacturing Letters

journal homepage: www.elsevier.com/locate/addlet

Development and characterization of a metastable Al-Mn-Ce alloy produced by laser powder bed fusion

Katharina Gabrysiak[a,*], Tobias Gustmann[a], Jens Freudenberger[a], Kai Neufeld[a], Lars Giebeler[a], Christoph Leyens[b,c], Uta Kühn[a]

[a] Institut of Complex Materials, Leibniz IFW Dresden, Helmholtzstr. 20, 01069 Dresden, Germany
[b] Institute of Materials Science, TU Dresden, Helmholtzstr. 7, 01069 Dresden, Germany
[c] Fraunhofer Institute for Material and Beam Technology (Fraunhofer IWS), Winterbergstr. 28, 01277 Dresden, Germany

ARTICLE INFO

Keywords:
Metastable aluminum alloys
Rapid solidification
Laser powder bed fusion
Mechanical characterization
$Al_{20}Mn_2Ce$

ABSTRACT

Laser powder bed fusion (LPBF) can help to overcome two challenges occurring by casting of metastable Al alloys: (1) the high amount of casting defects and (2) the limited part size while maintaining rapid solidification of the whole cross-section. In this study, an $Al_{92}Mn_6Ce_2$ alloy was processed crack-free without baseplate heating by LPBF. The high cooling rate during fabrication has a significant impact on the microstructure, which was characterized by SEM, TEM and XRD. The processing through LPBF causes a high amount and a strong refinement of the intermetallic $Al_{20}Mn_2Ce$ precipitates. This leads, compared to suction-cast specimens, to a higher hardness (180 HV 5) and a higher tolerable compressive stress (>1200 MPa) associated with a pronounced plasticity without failure up to a strain of 40%. The extraordinary mechanical properties of additively manufactured $Al_{92}Mn_6Ce_2$ can extend the possibilities of producing novel LPBF lightweight structures for potential applications under harsh conditions.

1. Introduction

Al alloys are widely used in lightweight structural applications because of their high specific strength. Conventional hardenable Al alloys show an ultimate tensile strength (σ_{UTS}) ranging from 100 MPa to 640 MPa [1]. Besides this, sophisticated processing techniques aiming at a refined microstructure are being applied to obtain even higher strength values. For instance Al-Zn-Mg-Cu alloys can reach a strength of 977 MPa through a nanostructural hierarchy after severe plastic deformation [2]. Another approach is the addition of Sc, which improves mechanical properties [3]. The high-performance Al-Mg-Sc-Zr alloy (Scalmalloy) shows an ultimate tensile strength of 520 MPa [4]. Scalmalloy has been developed for laser powder bed fusion processing (LPBF, also known as selective laser melting, SLM) with a focus on aerospace applications [3,5].

Contrary, the strength values for non-heat treatable Al alloys, such as the 3xxx alloys, are much lower (i.e. 100 MPa to 290 MPa [1]). These 3xxx alloys contain Mn as major alloying element and are generally strengthened by work hardening [1]. Beyond that, Al-Mn alloys were widely studied regarding their ability to form quasicrystals [6–8]. Numerous publications reported on the quasicrystal formation for rapidly solidified Al-Mn-Ce alloys as well [9–14], but meanwhile incorrect phase indication is assumed [15]. Recent investigations indicate the formation of the metastable fcc phase $Al_{20}Mn_2Ce$ instead of quasicrystals [16–20]. However, Al-Mn-Ce possesses remarkable mechanical properties, which make the material attractive for lightweight applications: high compressive strengths [9,13,21] (e.g. 800 MPa for $Al_{92}Mn_6Ce_2$ [18]), high hardness [17,18] up to 185 HV 5 for $Al_{94}Mn_4Ce_2$ [19] and improved mechanical stability at elevated temperatures [18] (e.g. 150 HV 5 at 400 °C for $Al_{92}Mn_4Ce_2$ [19]). Plotkowski et al. [19] manufactured $Al_{94}Mn_4Ce_2$ by LPBF with additional preheating of the baseplate. They determined an adequate tensile strength (≈ 260 MPa) and low tensile ductility at room temperature, but excellent strength retention exceeding that of Scalmalloy at 200 °C [19]. In order to understand the material behavior of the aforementioned alloys better, both analytical instruments as well as novel processing techniques have to be utilized to gather new insights into the complex phase formation.

Processing of metastable Al alloys can have significant drawbacks with respect to the supply of high-strength bulk materials. For instance, materials produced by rapid solidification technologies (e.g. melt spinning) are limited in their dimensions. Furthermore, many Al alloys including $Al_{92}Mn_6Ce_2$ suffer from casting defects (pores, cracks, segregations) [18,22]. Additive manufacturing techniques such as LPBF offer a great flexibility of producing individual geometries by local melting of thin powder layers. Additively manufactured Al alloys show an attractive combination of high specific strength (e.g. σ_{UTS}($AlSi_{10}Mg$, as-

* Corresponding author.
E-mail address: k.n.gabrysiak@ifw-dresden.de (K. Gabrysiak).

https://doi.org/10.1016/j.addlet.2021.100017
Received 22 September 2021; Received in revised form 22 October 2021; Accepted 25 October 2021
2772-3690/© 2021 The Authors. Published by Elsevier B.V. This is an open access article under the CC BY license (http://creativecommons.org/licenses/by/4.0/)

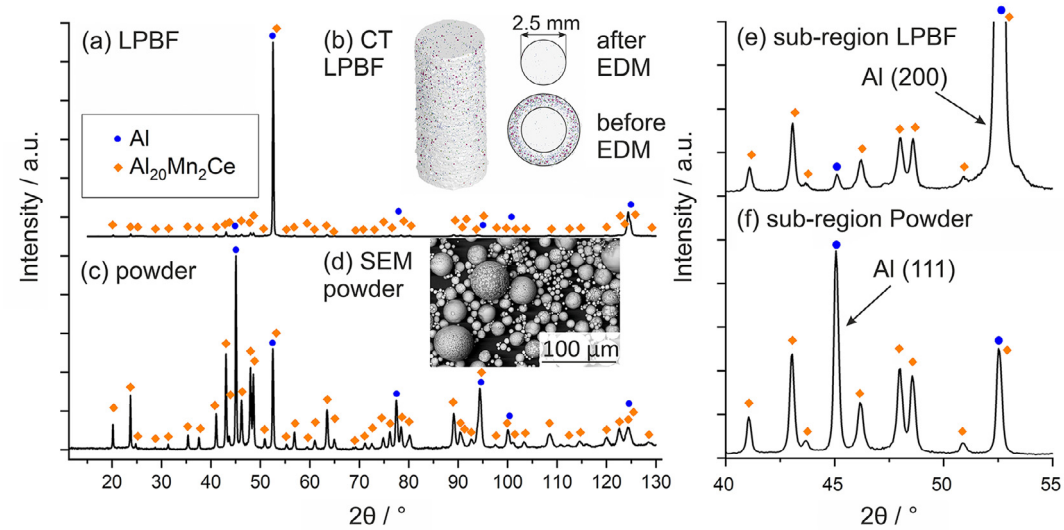

Fig. 1. (a) XRD pattern of the transversal section of a selected $Al_{92}Mn_6Ce_2$ LPBF sample (perpendicular to the building direction); (b) µCT-images showing residual pores (in red) in the as-built state and highly-dense samples after EDM; (c) XRD pattern of the as-atomized powder; (d) SEM micrograph thereof; (e, f) enlarged section of the respective diffraction patterns shown in a, c.

built) = 315 MPa [23] vs. σ_{UTS}($AlSi_{10}Mg$, as-cast) = 150 MPa [1]) and ductility due to high cooling rates [24–26]. The rapid solidification can lead to structural refinement and homogeneously distributed phases [27–30], supersaturation of the Al matrix [26,30,31] and metastable phases [18,30,31].

The main goal of our study is to give a better understanding of the process-microstructure-property-relationship of an $Al_{92}Mn_6Ce_2$ alloy processed by LPBF. In a first step (not deeply discussed here), adjusted process parameters were developed for the manufacturing of crack-free samples (diameter: around 4 mm, no baseplate heating applied). The focus of this work constitutes in the hierarchical microstructure induced by LPBF and its impact on the mechanical behavior. The mechanical properties are benchmarked against those obtained from suction cast thin rods. Overall, the use of LPBF is assessed for metastable bulk Al-Mn-Ce alloys, which cannot be fabricated through conventional casting.

2. Method and materials

Ingots with the nominal composition of $Al_{92}Mn_6Ce_2$ (at.%) were produced by induction melting of the raw materials (purities: Al 99.99%, Mn 99.7%, Ce > 99%). The spherical powder (Fig. 1(d)) was fabricated by means of the EIGA process (Electrode Induction Melting Inert Gas Atomization, Eckart TLS GmbH, Germany). The powder material was sieved to obtain a particle size range of 10 to 63 µm and analyzed via dynamic image analysis using a Camsizer X2 (Microtrac Retsch GmbH). The particle size distribution was found to be in the defined range (d_{10}: 15.9 µm, d_{50}: 35.9 µm, d_{90}: 57.3 µm). Cylindrical samples (diameter: 4 mm, height: 9 mm) were manufactured under Ar atmosphere using a SLM 250^{HL} machine (SLM Solutions Group AG, Germany). The laser power, scanning speed, hatching distance and layer thickness were 300 W, 1000 mm/s, 0.1 mm and 0.05 mm, respectively. For comparison, samples with the same composition (diameter: 4 mm, height: 75 mm) were produced by suction casting under Ar atmosphere using a water-cooled copper mold. A pre-validated piece of the rod (without pores and cracks) was chosen by means of X-ray computed tomography - µCT (voxel size: 6 µm, device: GE Phoenix Nanotom M) (Supplementary). Likewise, the quality and density of the LPBF samples was inspected by µCT.

The phases and crystallographic parameters were characterized by X-ray diffraction (XRD, PANalytical XPert Pro-PW3040/60, Co K_α, $\Delta 2\theta = 0.05°$) in Bragg-Brentano geometry. For Rietveld analysis [32], the sample was measured with a STOE Stadi P (Mo $K_{\alpha 1}$, curved Ge(111) single crystal monochromator, $\Delta 2\theta = 0.01°$) in transmission geometry. The Rietveld analysis of the XRD pattern was conducted with the FullProf Suite implemented in WinPlotR [33] (Supplementary). Microstructural analysis was carried out by scanning electron microscopy (SEM, Zeiss Leo 1530 Gemini). Furthermore, transmission electron microscopy (TEM, 200 kV, Philips Tecnai F20) and electron backscatter diffraction (EBSD, 20 kV, Bruker eFlash HD) were applied to investigate the microstructure. To examine the temperature-dependent phase transformation, differential scanning calorimetry measurements (DSC 7, Perkin Elmer) of four LPBF samples were conducted up to 630 °C. The heating and cooling rate were 20 K/min.

For compression tests, LPBF and cast samples with a height-to-diameter ratio of 1:1.5 – 2 were prepared according to DIN 50106. The LPBF samples were eroded to a diameter of 2.5 mm via electrical discharge machining (EDM) in order to exclude the influence of pores in surface near areas (Fig. 1(b)). All co-planar samples were additionally grinded (P1200) to reduce friction during testing. Four samples of each fabrication route were tested position-controlled using an electromechanical testing machine (Instron 8562) with an initial strain rate of 10^{-4} s^{-1}. The yield strength was determined through curve fitting (Avrami equation) of the elastic region. In this way, the maximum gradient was derived and taken as linear-elastic function. Furthermore, Vickers hardness was evaluated with a Mitutoyo ACK-C1 device applying a load of 49 N for 10 s (HV 5). In addition, microhardness was measured using a load of 0.196 N for 10 s (HV 0.01, HMV Shimadzu).

3. Results and discussion

The XRD patterns of the as-atomized powder and the LPBF sample are shown in Fig. 1. Both samples contain two main crystalline phases: Al in the space group Fm-3m and $Al_{20}Mn_2Ce$ in the space group Fd-3m. The $Al_{20}Mn_2Ce$ structure, which was reported by Gordillo [17], was derived from the $Al_{18}Mg_3Cr_2$ structure type [34,35].

The Rietveld analysis of the powder reveals a lattice parameter of 14.4285(5) Å for $Al_{20}Mn_2Ce$ and of 4.0433(2) Å for Al. The diffraction pattern of the LPBF sample exhibits very strong 200 and 400 reflections

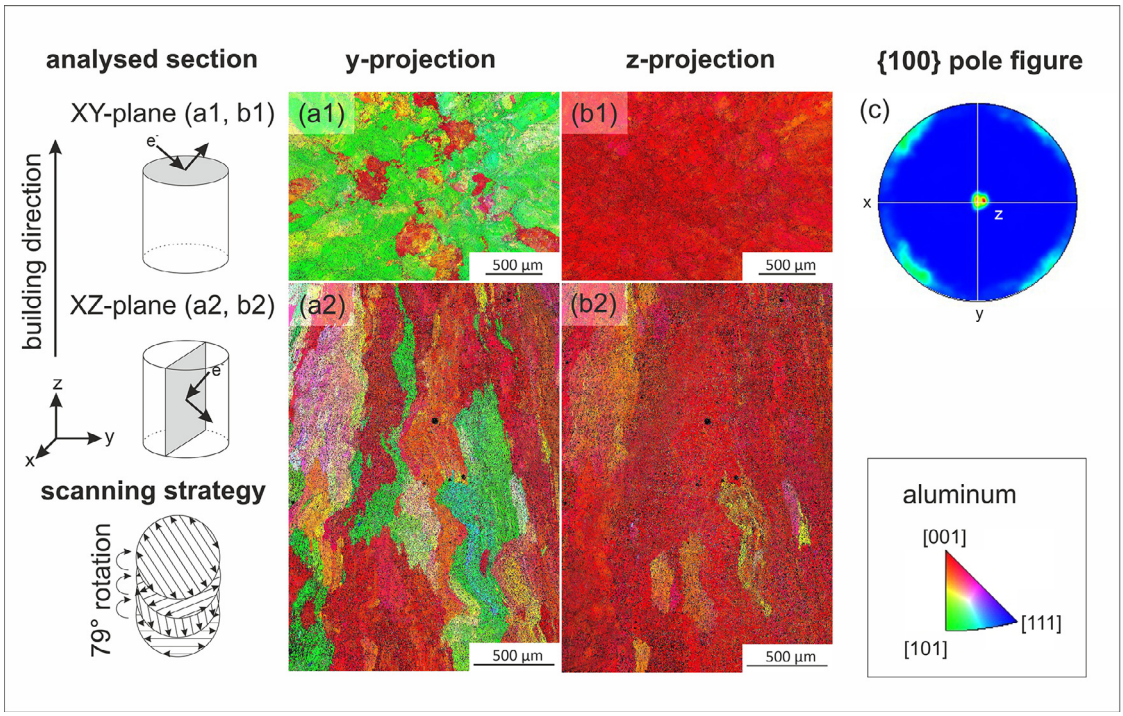

Fig. 2. IPF maps of the Al matrix (LPBF). The XY (transversal section) and XZ-plane (longitudinal section) as (a) y-projection and (b) z-projection. (c) pole figure with preferred orientation of {100} in building direction. The LPBF scanning strategy is visualized as top view: the melt track direction rotates 79° every layer.

of the Al phase at $2\theta = 52.5^\circ$ and 124.4° due to a substantial {100} texture related to the building direction. It shows additional unindexed reflections from minor phases. They may be related to Fe impurities from powder processing, to complex nanocrystalline phases or to artefacts due to sample preparation.

The µCT image of the LPBF sample in Fig. 1(b) illustrates pores at the surface near areas. This can be traced to the fact that skywriting is not available for the used SLM setup and hot spots for shorter scan vectors (rod, center-to-edge movement) and pore trapping can occur [36]. Please note, that the overall area content of pores is relatively small irrespective of the visual appearance due to the parallel prospective. The density measured by µCT in the as-built state and after EDM reaches 99.95% and close to 100%, respectively (pores smaller than 11 µm are not considered). The sample after EDM presents an almost defect-free counterpart to the selected cast specimen (Supplementary).

Fig. 2 shows the inverse pole figure (IPF) maps of the Al matrix at a low magnification. Data was separately acquired from horizontal (a1, b1) and longitudinal (a2, b2) planes based on the sample coordinate system. The z-projections (Fig. 2(b1, b2) and the pole figure (Fig. 2(c1)) confirm the preferred {100} orientation in the building direction. Consequently, orientations spreading the range between {100} and {110} are present in x and y direction. As can be seen from the longitudinal section (Fig. 2(a2)), the Al grains are elongated along the building direction and possess a length within the mm range.

In order to analyze the structure of the LPBF samples, observations at multiple scales are necessary (Fig. 3). At mesoscale (Fig. 3(a1, b1)), the microstructure is dominated by elongated Al-grains, which appear equiaxial in the transversal section. An Al-grain consists of several melt tracks with a width of about 250 µm (Fig. 3(a2)). This implies that Al grows epitaxially over several processed layers. The tracks do not exhibit any chemical inhomogeneities (Energy-dispersive X-ray spectroscopy (EDX) results not shown here). Instead, they are observable due to the varying morphology of $Al_{20}Mn_2Ce$ (Fig. 3(b2)). In Fig. 3(a3, b3) the different laser impact zones of the melt track are described. The solidification starts in zone 2, where the material is remelted and forms elongated dendrites towards the heat flow. The solidification continues towards the center (zone 1), where precipitates with a rosette-like morphology are found. The melt pool boundary is marked as zone 3. Beyond this region a heat treatment occurs resulting in a coarsening of the $Al_{20}Mn_2Ce$ precipitates (zone 4).

Fig. 4(a) displays the melt pool further examined by TEM. The diffraction pattern of the precipitates (Fig. 4(d)) confirms the XRD results by revealing the $Al_{20}Mn_2Ce$ phase. DSC analyses (Fig. 4(b)) verify the metastable state of this phase. The phase transformation temperature of $T_{onset} = 414 \pm 27$ °C is similar to what has been observed for the formerly supposed quasicrystals [37]. The dimension of the rosettes and dendrites ranges from 500 nm to 2 µm, whereas the individual $Al_{20}Mn_2Ce$ grains are 100 – 500 nm (Fig. 4(c)). Furthermore, some globular particles with the size of 20 nm were found, which could not be clearly identified due to their small expanse and content (Fig. 4(a)). Those particles contain a high amount of Ce, measured by EDX at TEM (not shown here), suggesting the $Al_{11}Ce_3$ phase. This presumption is substantiated by literature [17–19] and could explain the endothermic peak at the DSC through an eutectic reaction (Fig. 4(b)).

The $Al_{20}Mn_2Ce$ phase is strongly twinned as depicted in Fig. 4(a, c). The indexing of the electron diffraction pattern (Fig. 4(d)) was conducted by the software Single Crystal 4.1 simulating the $Al_{20}Mn_2Ce$ structure. The analysis exhibits {111} twins as commonly known for fcc materials and already reported for this phase [18]. A possible reason for the striking high amount of twins is the high cooling rate during LPBF within the range of 10^4 to 10^6 K/s [38–40]. The rapid solidification leads to a metastable microstructure irrespective of the number of repetitive laser scans. This also causes a lattice distortion of the Al matrix due to lattice defects (Fig. 4(a)). Moreover, $Al_{20}Mn_2Ce$ is known to solidify preferably at high cooling rates [18].

The LPBF samples possess a Vickers hardness of 161 – 179 HV 5, which is about 20% higher compared to the suction cast samples (130 – 138 HV 5; Table 1). The reason lies in the high cooling rates during LPBF, which lead to the formation of smaller $Al_{20}Mn_2Ce$ precipitates (up to 500 nm) compared to the as-cast state (up to 4 µm) (Fig. 5). Furthermore, the microhardness of the LPBF specimens varies within the melt track. The center with finer intermetallic grains reveals a

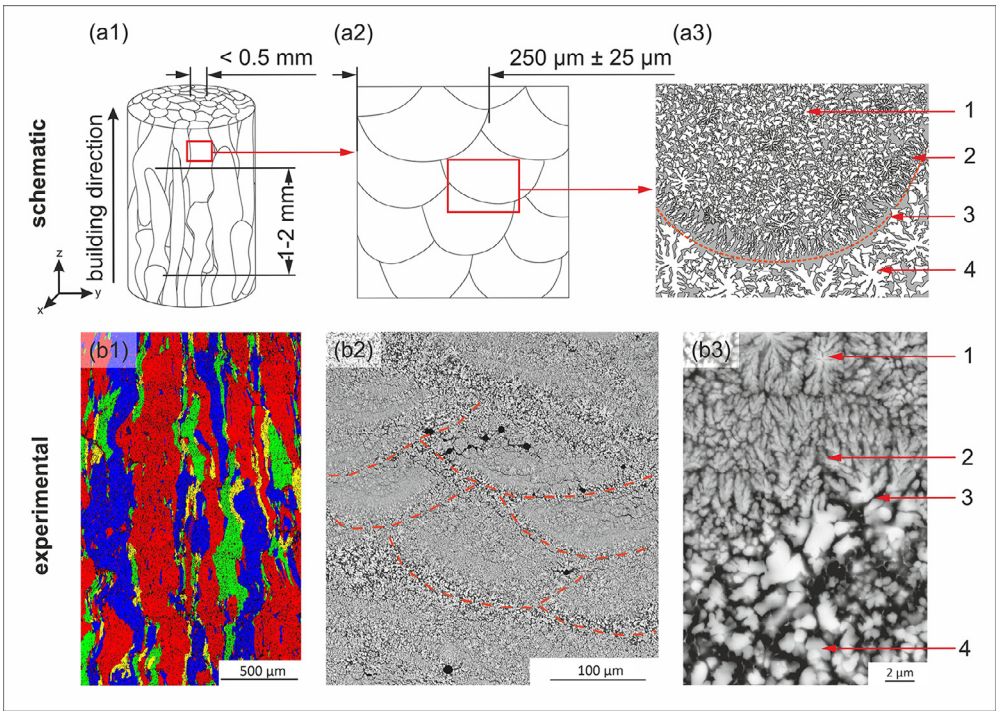

Fig. 3. (a) Schematic illustration of the longitudinal LPBF microstructure at different length scales and (b) corresponding EBSD grain map and SEM images. (a1/b1): elongated Al-grains, (a2/b2): solidified melt pools indicating a track width of around 250 µm, (a3/b3): morphology of the $Al_{20}Mn_2Ce$ phase across the former laser scan tracks. Track zones as indexed in a3 and b3: 1) center of the melt track, 2) directional solidified region, 3) melt pool boundary and 4) heat-affected zone below.

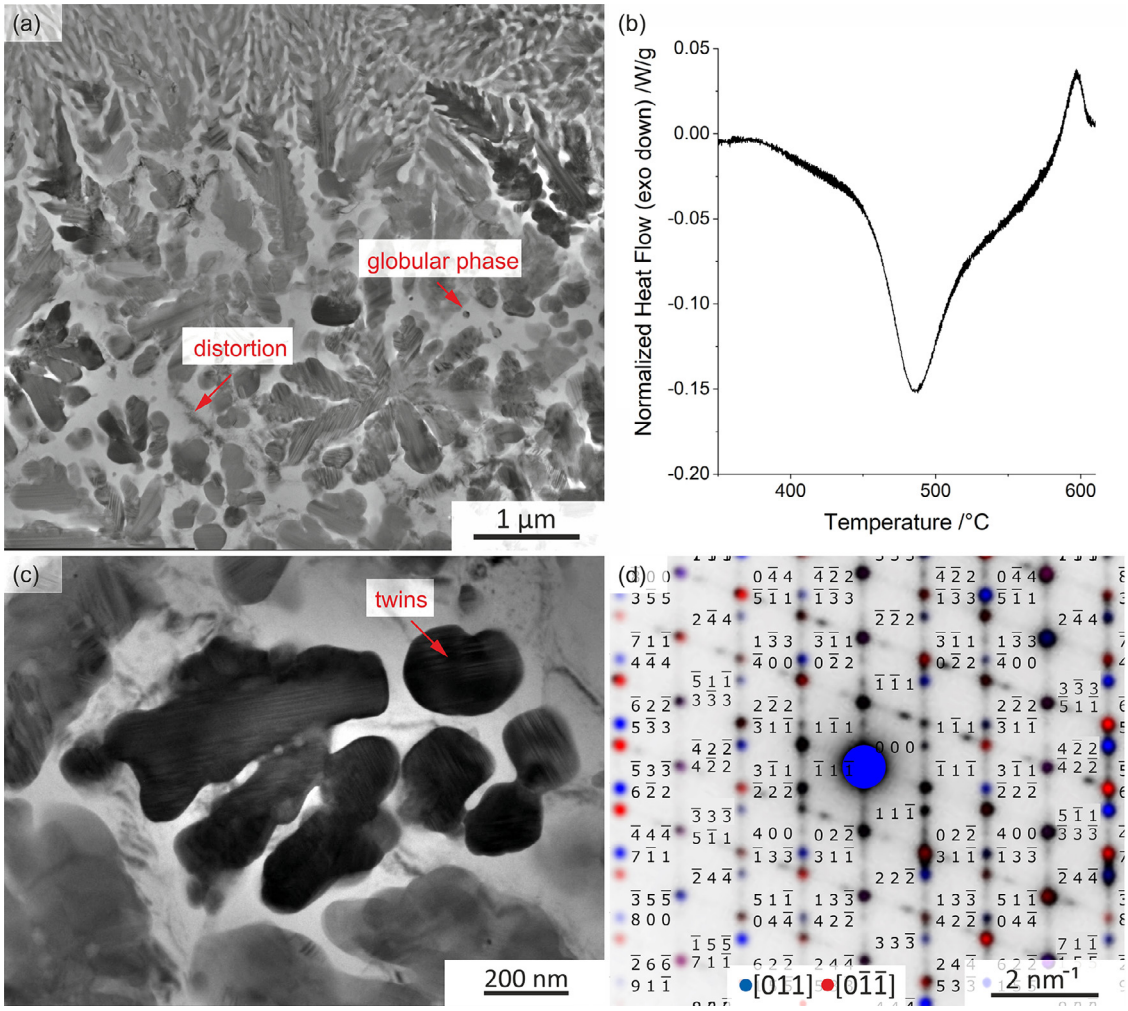

Fig. 4. (a) TEM images of a LPBF specimen showing $Al_{20}Mn_2Ce$ precipitates and a distorted Al-matrix, (b) DSC measurement of the irreversible phase transformation during heating, (c) twinned $Al_{20}Mn_2Ce$ (d) section of the corresponding electron diffraction pattern with indexed {111} twinning and superimposed simulated pattern of $Al_{20}Mn_2Ce$.

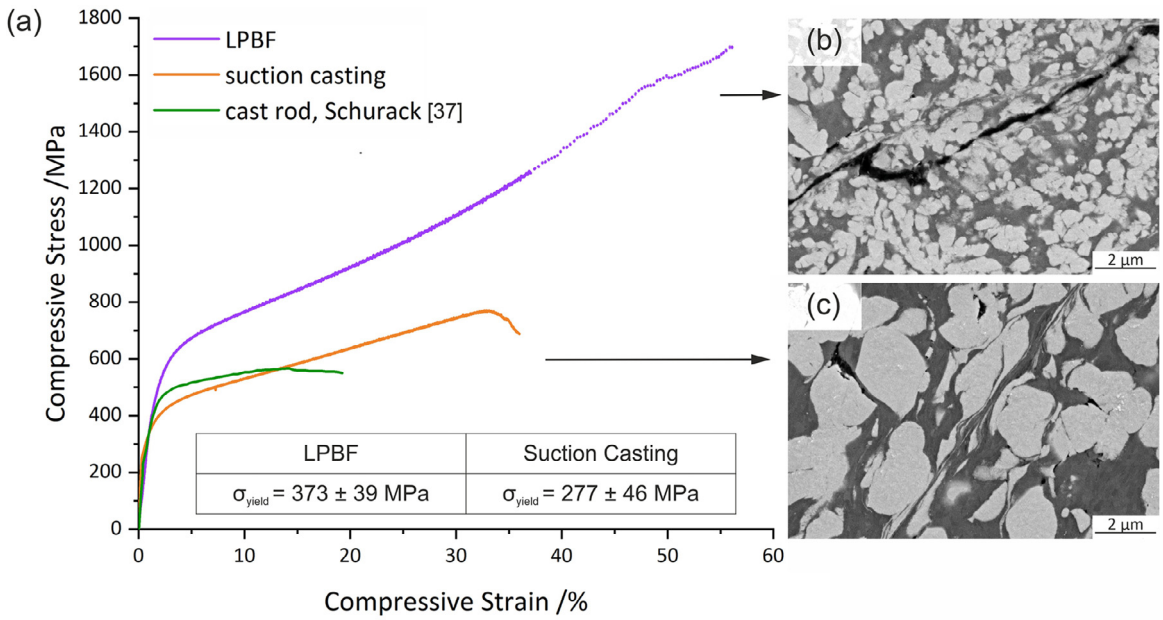

Fig. 5. (a) Compressive stress-strain curves of $Al_{92}Mn_6Ce_2$ processed by LPBF and casting. For comparison, the compression curve of a cast rod with the same composition is taken from [37].The dotted curve describes the compression behavior of the LPBF sample after exceeding the abort criterion (at 37% strain, where sample height = diameter). Corresponding SEM-micrograph after testing of (b) LPBF processed and (c) suction cast sample.

Table 1
Macro- and microhardness of $Al_{92}Mn_6Ce_2$ as-built(LPBF) and as-cast. The number in parentheses implies the overall number of applied indentations.

Macrohardness	LPBF	Suction Casting
XY-plane (transversal section)	179 HV 5 ± 5 (10)	130 HV 5 ± 6 (10)
XZ-plane (longitudinal section)	161 HV 5 ± 6 (10)	137.5 HV 5 ± 1.9 (10)
Microhardness melt track		
Heat affected zone	168 HV 0.01 ± 14 (25)	–
Center	228 HV 0.01 ± 36 (25)	–

hardness that is about 25% higher in comparison with the heat-affected zone.

The hardness results of the cast specimen are similar to those of former studies [18,19]. However, the microhardness of LPBF generated $Al_{92}Mn_6Ce_2$ samples is higher compared to other Al-alloys produced by LPBF (e.g. 95 HV 0.01 for $AlSi_{12}$ [41], 127 HV 0.5 for $AlSi_{10}Mg$ [42], 161 HV 0.3 for heat-treated Scalmalloy [43]). This indicates a high resistance of refined $Al_{20}Mn_2Ce$ against local deformation.

Fig. 5(a) shows stress-strain curves measured in compression of a LPBF and a cast specimen. Even though both exhibit a similar rate of strain hardening, the LPBF specimen shows higher stress values and is capable of a larger plastic strain compared to the cast sample. The LPBF sample comprises a compressive yield strength (σ_{yield}) of 373 ± 39 MPa, which is around 100 MPa above that of the cast sample. Moreover, it withstands an engineering stress in compression of at least 1200 MPa without failure, whereas the cast counterpart attains an ultimate compressive stress (σ_{UCS}) of 760 ± 37 MPa. In addition, the LPBF sample does not fail until the abort criterion of the test (diameter = height), which is equivalent to a strain of approximately 40%. As already discussed, the smaller intermetallic precipitates lead to a significant increase in strength of the additively manufactured material. Fig. 5(b, c) displays the deformation propagation and the fragmented $Al_{20}Mn_2Ce$ precipitates of a LPBF and a cast sample after testing. The investigation of the perplexing high ductility requires a more detailed analysis of the dislocation network of tensile tested material which is beyond the scope of the present article.

The compression behavior of the cast $Al_{92}Mn_6Ce_2$ is only roughly comparable to values of former publications. Coury et al. [18] observed similar values compared to our investigations (σ_{yield} = 302 MPa, σ_{UCS}= 800 MPa, ε_f = 30%), whereas the differing results of Schurack et al. [9,37] are illustrated in Fig. 5(a) (σ_{yield} = 392 MPa, σ_{UCS} = 565 MPa, ε_f = 19%). Discrepancies between these studies can be traced to different cast conditions causing disparately sized $Al_{20}Mn_2Ce$ precipitates. Also, the appearance of casting defects, as pores in [18], lead to a smaller effective sample area and thus to lower strength. The deviation of the compressive yield strength can also result from different ways of data evaluation. Regarding the data of Schurack et al. (Fig. 5(a) [37]), it can be seen, that the transition from the elastic to the plastic behavior occurs at a lower stress compared to the LPBF sample. Despite this, a lower yield strength for the LPBF specimen ($\sigma_{yield,\ Schurack}$ = 392 MPa vs. $\sigma_{yield,LPBF}$ = 373 MPa) was determined, demonstrating the limited comparability of yield strength values. Nevertheless, the approach of curve fitting was chosen to analyze the yield strength, as we are convinced, that this method is more exact and independent of the operator.

The compression test results of the LPBF sample perform well compared to other Al alloys produced by LPBF. Scalmalloy shows lower stress and strain values than $Al_{92}Mn_6Ce_2$, but a higher yield strength in the hot isostatic pressed and aged condition (σ_{yield} = 431 MPa, σ_{UCS} = 920 MPa, ε_f = 39% [44]). Thus, the $Al_{92}Mn_6Ce_2$ alloy withstands high stress through finely dispersed $Al_{20}Mn_2Ce$ precipitates and the solution hardened Al matrix without any post treatment.

4. Conclusions

This study demonstrates the successful processing of $Al_{92}Mn_6Ce_2$ by laser powder bed fusion without preheating the baseplate. The applied process parameters result in a unique microstructure modification, characterized by a relative coarse-grained fcc Al matrix and a submicrometer fcc $Al_{20}Mn_2Ce$ phase. The high cooling rate causes a high amount and a strong refinement of metastable $Al_{20}Mn_2Ce$. This phase combination and the layered microstructure lead to remarkable mechanical properties, such as high hardness (160 – 180 HV 5), high tolerable compression stress (> 1200 MPa) and strain (> 40%) values.

In contrast to conventional casting techniques, LPBF enables the production of almost defect-free bulk $Al_{92}Mn_6Ce_2$ samples. Their mechanical performance in the as built-state exceeds many conventional Al alloys and thus, offers a high potential for very demanding lightweight applications. To achieve a better overview of the processability of $Al_{92}Mn_6Ce_2$, we will further study the impact of the sample geometry and additional preheating on the part quality in the near future. This will be an important milestone to produce, for instance, tensile samples and to envisage the fabrication of prototypes.

Declaration of Competing Interest

The authors declare that they have no known competing financial interests or personal relationships that could have appeared to influence the work reported in this paper.

Funding/ Acknowledgement

This work was supported by the German Science Foundation (DFG) under grant KU 1974/15–1.

The authors would like to thank S. Donath, K. Baumgart, A. Voß, H. Bußkamp, R. Keller, N. Geißler, B. Bartusch, and A. Hariharan for technical assistance and they are grateful to F. Palm (Airbus Group) for scientific support.

Supplementary materials

Supplementary material associated with this article can be found, in the online version, at doi:10.1016/j.addlet.2021.100017.

References

[1] F. Ostermann, Anwendungstechnologie Aluminium, Springer Vieweg, Berlin, Heidelberg, 2014.
[2] P.V. Liddicoat, X.-.Z. Liao, Y. Zhao, Y. Zhu, M.Y. Murashkin, E.J. Lavernia, R.Z. Valiev, S.P. Ringer, Nanostructural hierarchy increases the strength of aluminium alloys, Nat. Commun. 1 (1) (2010) 63.
[3] S. Gialanella, A. Malandruccolo, Aerospace Alloys, 1st ed., Springer, 2020.
[4] APWORKS, Material Data Sheet –Scalmalloy®, 2017. https://www.apworks.de/scalmalloy. (Accessed 26.08. 2021).
[5] K. Schmidtke, F. Palm, A. Hawkins, C. Emmelmann, Process and mechanical properties: applicability of a scandium modified Al-alloy for laser additive manufacturing, Physics Procedia 12 (2011) 369–374.
[6] D. Shechtman, I. Blech, D. Gratias, J.W. Cahn, Metallic phase with long-range orientational order and no translational symmetry, Phys. Rev. Lett. 53 (20) (1984) 1951–1953.
[7] R.D. Field, H.L. Fraser, Precipitates possessing icosahedral symmetry in a rapidly solidified AlMn alloy, Mater. Sci. Eng. 68 (2) (1985) L17–L21.
[8] A. Inoue, L. Arnberg, B. Lehtinen, M. Oguchi, T. Masumoto, Compositional analysis of the icosahedral phase in rapidly quenched Al-Mn and Al-V alloys, Metall. Mater. Trans. A 17 (10) (1986) 1657–1664.
[9] F. Schurack, J. Eckert, L. Schultz, Al-Mn-Ce quasicrystalline composites: phase formation and mechanical properties, Philos. Mag. 83 (7) (2003) 807–825.
[10] M. Watanabe, A. Inoue, H. Kimura, T. Aiba, T. Masumoto, High Mechanical Strength of Rapidly Solidified Al92Mn6Ln2 (Ln=Lanthanide Metal) Alloys with Finely Mixed Icosahedral and Al Phases, Mater. Trans. 34 (1993) 162–168 JIM.
[11] R. Nicula, A. Jianu, G. Holzhüter, T. Barfels, E. Burkel, Grain-Size Refinement in Al-Mn-Ce Rapidly-Quenched Alloys, Mater. Sci. Forum 343-346 (2000) 27–32.
[12] R. Manaila, D. Macovei, R. Popescu, A. Devenyi, A. Jianu, E. Vasile, P.B. Barna, J.L. Lábár, Nano-icosahedral Al–Mn–Ce phases: structure and local configurations, Mater. Sci. Eng. 294-296 (2000) 82–85.
[13] J.-.H. Jun, J.-.M. Kim, K.-.T. Kim, W.-.J. Jung, Fabrication and mechanical properties of quasicrystal-reinforced AlMnMm alloys, Mater. Sci. Eng. 449-451 (2007) 979–982.
[14] A. Inoue, M. Watanabe, H. Kimura, F. Takahashi, A. Nagata, T. Masumoto, High Mechanical Strength of Quasicrystalline Phase Surrounded by fcc-Al Phase in Rapidly Solidified Al-Mn-Ce Alloys, Mater. Trans. JIM 33 (1992) 723–729.
[15] F.G. Coury, W.J. Botta, C. Bolfarini, C.S. Kiminami, M.J. Kaufman, Reassessment of the effects of Ce on quasicrystal formation and microstructural evolution in rapidly solidified Al–Mn alloys, Acta Mater. 98 (2015) 221–228.
[16] S. Mula, S. Ghosh, S.K. Pabi, On the formation of phases by mechanical alloying and their thermal stability in Al–Mn–Ce system, Powder Technol. 191 (1) (2009) 176–181.
[17] M.A. Gordillo, I. Cernatescu, T.T. Aindow, T.J. Watson, M. Aindow, Phase stability in a powder-processed Al–Mn–Ce alloy, J. Mater. Sci. 49 (10) (2014) 3742–3754.
[18] F.G. Coury, C.S. Kiminami, W.J. Botta, C. Bolfarini, M.J. Kaufman, Design and production of Al-Mn-Ce alloys with tailored properties, Mater Design 110 (2016) 436–448.
[19] A. Plotkowski, K. Sisco, S. Bahl, A. Shyam, Y. Yang, L. Allard, P. Nandwana, A.M. Rossy, R.R. Dehoff, Microstructure and properties of a high temperature Al–Ce–Mn alloy produced by additive manufacturing, Acta Mater. 196 (2020) 595–608.
[20] Y. Yang, S. Bahl, K. Sisco, M. Lance, D. Shin, A. Shyam, A. Plotkowski, R.R. Dehoff, Primary solidification of ternary compounds in Al-rich Al–Ce–Mn alloys, J. Alloys Compd. 844 (2020) 156048.
[21] F. Schurack, J. Eckert, L. Schultz, Quasicrystalline Al-alloys with high strength and good ductility, Mater. Sci. Eng. 294-296 (2000) 164–167.
[22] M. Di Sabatino, L. Arnberg, Castability of aluminium alloys, Trans. Indian Inst. Met. 62 (4) (2009) 321–325.
[23] J.H. Martin, B.D. Yahata, J.M. Hundley, J.A. Mayer, T.A. Schaedler, T.M. Pollock, 3D printing of high-strength aluminium alloys, Nature 549 (7672) (2017) 365–369.
[24] N.T. Aboulkhair, I. Maskery, C. Tuck, I. Ashcroft, N.M. Everitt, The microstructure and mechanical properties of selectively laser melted AlSi10Mg: the effect of a conventional T6-like heat treatment, Mater. Sci. Eng. 667 (2016) 139–146.
[25] N.E. Uzan, S. Ramati, R. Shneck, N. Frage, O. Yeheskel, On the effect of shot-peening on fatigue resistance of AlSi10Mg specimens fabricated by additive manufacturing using selective laser melting (AM-SLM), Add. Manuf. 21 (2018) 458–464.
[26] X.P. Li, X.J. Wang, M. Saunders, A. Suvorova, L.C. Zhang, Y.J. Liu, M.H. Fang, Z.H. Huang, T.B. Sercombe, A selective laser melting and solution heat treatment refined Al–12Si alloy with a controllable ultrafine eutectic microstructure and 25% tensile ductility, Acta Mater. 95 (2015) 74–82.
[27] B. Basu, A.W. Date, Rapid solidification following laser melting of pure metals—II. Study of pool and solidification characteristics, Int. J. Heat Mass Transfer 35 (5) (1992) 1059–1067.
[28] E. Karaköse, M. Keskin, Effect of solidification rate on the microstructure and microhardness of a melt-spun Al–8Si–1Sb alloy, J. Alloys Compd. 479 (1) (2009) 230–236.
[29] M.Â.O. de Alfaia, R. Oliveira, T.S. Lima, F.E. Mariani, L.C. Casteletti, N. Cheung, A. Garcia, Effects of cooling rate and microstructure scale on wear resistance of unidirectionally solidified Al-3.2wt.%Bi-(1; 3) wt.%Pb alloys, Materials Today Commun. 25 (2020) 101659.
[30] N.T. Aboulkhair, M. Simonelli, L. Parry, I. Ashcroft, C. Tuck, R. Hague, 3D printing of aluminium alloys: additive manufacturing of aluminium alloys using selective laser melting, Prog. Mater Sci. 106 (2019) 100578.
[31] E.J. Lavernia, T.S. Srivatsan, The rapid solidification processing of materials: science, principles, technology, advances, and applications, J. Mater. Sci. 45 (2) (2010) 287–325.
[32] H.M. Rietveld, A profile refinement method for nuclear and magnetic structures, J. Appl. Crystallogr. 2 (2) (1969) 65–71.
[33] T. Roisnel, J. Rodríquez-Carvajal, WinPLOTR: a windows tool for powder diffraction pattern analysis, Mater. Sci. Forum 378-381 (2001) 118–123.
[34] S. Samson, Crystal structure of the intermetallic compound Mg3Cr2Al18, Nature 173 (4416) (1954) 1185–1186.
[35] S. Samson, The crystal structure of the intermetallic compound Mg3Cr2Al18, Acta Crystallogr. 11 (12) (1958) 851–857.
[36] S.A. Khairallah, A.T. Anderson, A. Rubenchik, W.E. King, Laser powder-bed fusion additive manufacturing: physics of complex melt flow and formation mechanisms of pores, spatter, and denudation zones, Acta Mater. 108 (2016) 36–45.
[37] F. Schurack, J. Eckert, L. Schultz, Synthesis and mechanical properties of cast quasicrystal-reinforced Al-alloys, Acta Mater. 49 (8) (2001) 1351–1361.
[38] S. Pauly, P. Wang, U. Kühn, K. Kosiba, Experimental determination of cooling rates in selectively laser-melted eutectic Al-33Cu, Additive Manuf. 22 (2018) 753–757.
[39] M. Tang, P.C. Pistorius, S. Narra, J.L. Beuth, Rapid Solidification: selective Laser Melting of AlSi10Mg, JOM 68 (3) (2016) 960–966.
[40] Y. Li, D. Gu, Parametric analysis of thermal behavior during selective laser melting additive manufacturing of aluminum alloy powder, Mater Design 63 (2014) 856–867.
[41] K.G. Prashanth, R. Damodaram, S. Scudino, Z. Wang, K.Prasad Rao, J. Eckert, Friction welding of Al–12Si parts produced by selective laser melting, Mater Design 57 (2014) 632–637.
[42] A. Iturrioz, E. Gil, M.M. Petite, F. Garciandia, A.M. Mancisidor, M. San Sebastian, Selective laser melting of AlSi10Mg alloy: influence of heat treatment condition on mechanical properties and microstructure, Welding World 62 (4) (2018) 885–892.
[43] L. Cordova, T. Bor, M. de Smit, S. Carmignato, M. Campos, T. Tinga, Effects of powder reuse on the microstructure and mechanical behaviour of Al–Mg–*Sc*–Zr alloy processed by laser powder bed fusion (LPBF), Add. Manuf. 36 (2020) 101625.
[44] F. Palm, Values are provided by personal communication and released for publication.